

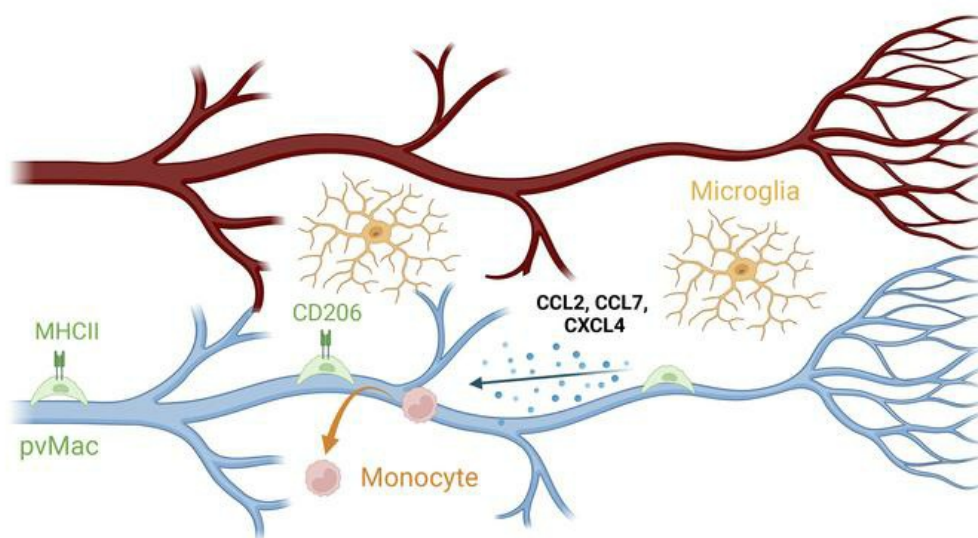
Retinal perivascular macrophages regulate immune cell infiltration during neuroinflammation in mouse models of ocular disease

Jacob K. Sterling, ... , C. Elyse Brookins, Jeremy A. Lavine

J Clin Invest. 2024. <https://doi.org/10.1172/JCI180904>.

Research In-Press Preview Ophthalmology

Graphical abstract



Find the latest version:

<https://jci.me/180904/pdf>



Retinal perivascular macrophages regulate immune cell infiltration during neuroinflammation in mouse models of ocular disease

Jacob K. Sterling^{1,2,3*}, Amrita Rajesh^{3*}, Steven Droho³, Joyce Gong³, Andrew L. Wang³, Andrew P. Voigt³, C. Elysse Brookins³, Jeremy A. Lavine³

¹Department of Medicine, Feinberg School of Medicine, Northwestern University, Chicago, IL, USA

²Physician Scientist Track Program, Internal Medicine Residency, Northwestern University, Chicago, IL, USA

³Department of Ophthalmology, Feinberg School of Medicine, Northwestern University, Chicago, IL, USA

* JKS and AR contributed equally to this study. Jacob K Sterling was chosen as the first author, despite equal overall contribution with Amrita Rajesh, due to his role in conceptualization and writing of the original draft.

Corresponding Author:

Jeremy A. Lavine MD PhD

240. E. Huron St., McGaw M343

Chicago, IL 60614

312-503-4733

jeremy.lavine@northwestern.edu

ORCID: 0000-0002-0884-1336

Running Title: Perivascular macrophages regulate immune cell infiltration.

JAL is a consultant for Line 6 Biotechnology and Genentech. JAL received research grant support from Therini Bio. No company body had any role in the design of the study, collection, analysis, interpretation of data, or in writing the manuscript. The authors have no additional financial interests.

Abstract

The blood-retina barrier (BRB), which is disrupted in diabetic retinopathy (DR) and uveitis, is an important anatomical characteristic of the retina, regulating nutrient, waste, water, protein, and immune cell flux. The BRB is composed of endothelial cell tight junctions, pericytes, astrocyte end feet, a collagen basement membrane, and perivascular macrophages. Despite the importance of the BRB, retinal perivascular macrophage function remains unknown. We found that retinal perivascular macrophages reside on post-capillary venules in the superficial vascular plexus and express MHCII. Using single-cell RNA-sequencing, we found that perivascular macrophages express a pro-chemotactic transcriptome and identified *Pf4/CXCL4* as a perivascular macrophage marker. We used *Pf4^{Cre}* mice to specifically deplete perivascular macrophages. To model retinal inflammation, we performed intraocular CCL2 injections. Ly6C⁺ monocytes crossed the BRB proximal to perivascular macrophages. Depletion of perivascular macrophages severely hampered Ly6C⁺ monocyte infiltration. These data suggest that retinal perivascular macrophages orchestrate immune cell migration across the BRB, with implications for inflammatory ocular diseases including DR and uveitis.

Introduction

The blood vessels of the central nervous system (CNS) possess unique properties which allow them to regulate the flux of molecules and cells between the systemic circulation and the tightly controlled environment of the CNS. The blood-retina barrier (BRB), which is analogous to the blood-brain barrier, is an important anatomical characteristic of the retina, regulating nutrient, waste, water, protein, and immune cell flux. Disruption of the BRB leads to vasogenic edema, immune cell infiltration, and neurodegeneration across multiple ocular diseases. In diabetic retinopathy (DR) for example, BRB disruption leads to leaky vasculature, and correlates with DR severity (1). In retinal-involving non-infectious and infectious uveitis, BRB dysfunction is exemplified by cystoid macular edema with petaloid leakage, fern-like retinal vasculitis in intermediate uveitis, Kyrieleis Plaques in Toxoplasmosis, and potentially Gass Plaques in Susac Syndrome (2).

At the cellular and molecular level, the BRB is composed of endothelial cell tight junctions, pericytes, astrocyte end feet, a Collagen IV basement membrane, and perivascular macrophages (3). While many studies have interrogated the function of the BRB, and its individual components, retinal perivascular macrophages are under-investigated, and their function remains largely unknown. Perivascular macrophages were first noted in the literature in the 1950s (4). Subsequent work to identify the function of these cells has been limited. In 2009, one manuscript demonstrated that IBA1^{neg}F4/80⁺CD11b⁺ macrophages, which were described as perivascular macrophages, migrate along blood vessels to sites of BRB breakdown (5). Since the late 2000s, select publications have noted changes in possible perivascular macrophage

morphology and number in mouse models of DR (6), retinal vein occlusion (7), and light damage (8). Of note, the markers used in these studies to identify perivascular macrophages included CD14, F4/80, and IBA1, which are inadequate to differentiate perivascular macrophages from infiltrating monocytes and monocyte-derived macrophages.

Compared to retinal perivascular macrophages, brain perivascular macrophages have been studied in greater detail. Recent landmark publications have shown that brain perivascular macrophages are derived from meningeal macrophages, which are yolk sac- and fetal liver-derived, without contribution from the bone marrow. In the adult mouse, brain perivascular macrophages occupy a unique niche within the collagen IV basement membrane of both venules and arterioles, but not capillaries, forming a critical piece of the blood-brain barrier (9). The potential functions of brain perivascular macrophages include maintenance of the blood-brain barrier, and mediation of neurovascular and cognitive dysfunction during both hypertension and Alzheimer's Disease, which are associated with blood-brain barrier hyperpermeability (3, 10).

Previous work has shown that outside the CNS, blood vessel-associated macrophages mediate immune cell recruitment via cross talk with endothelial cells (11). In addition, immune cell recruitment occurs at post-capillary venules and not capillaries (12). Given the physical proximity of retinal perivascular macrophages and retinal endothelial cells, and the aforementioned links between BRB dysfunction and peripheral immune cell recruitment, we hypothesized that retinal perivascular macrophages regulate immune cell infiltration during neuroinflammation.

We previously showed that retinal perivascular macrophages are identifiable in the mouse retina as $Tmem119^{neg}CD206^{+}IBA1^{+}$ elongated cells that are adjacent to $CD31^{+}$ vessels and within the Collagen IV perivascular sheath (13). In this study, we investigated the anatomical locations of retinal perivascular macrophages, identified a mouse model to target them, used prior single-cell RNA-sequencing data to infer perivascular macrophage function, and tested whether their ablation impacted neuroinflammation. We found that retinal perivascular macrophages reside on post-capillary venules, can be targeted with *Pf4^{Cre}* mice, express a pro-chemotactic transcriptional profile, and their ablation decreases immune cell infiltration during acute neuroinflammation. Together these data point to perivascular macrophages as key mediators of retinal inflammation, a pathogenic feature of multiple retinal inflammatory and degenerative diseases.

Results

To comprehensively characterize perivascular macrophages, we performed multiparameter flow cytometry of retina from *Tmem119^{GFP/+}* mice, which label microglia GFP^{+} with high sensitivity in the brain and retina (13, 14). After singlet gating, live, $CD45^{+}$ cells were gated forward (Fig 1A left). Next, $CD11b^{+}Lineage^{neg}$ (Lineage = B-cells, T-cells, NK cells, eosinophils, and neutrophils) cells were isolated (Fig 1A, top middle). $CD64$ was used to identify all macrophages (Fig 1A, bottom middle). Microglia were defined as $Cx3cr1^{high}GFP^{+}$ cells (Fig 1A, top right). We used $CD169$ to discriminate vitreal hyalocytes on the surface of the retina from perivascular macrophages (13, 15). We defined perivascular macrophages as $CD206^{dim}CD169^{neg}$ and hyalocytes as $CD206^{+}CD169^{+}$ from non-microglia macrophages (Fig 1A, bottom right). The fluorescence minus one

(FMO) control for CD169 is shown in Fig S1. Quantitative analysis confirmed that perivascular macrophages were CD206^{dim} (Fig 1B-C) and expressed very low levels of CD169 compared to hyalocytes (Fig 1D-E). Quantitative analysis of cell counts per mouse revealed that perivascular macrophages were the second most abundant macrophage subtype in the retina (Fig 1F).

Next, we performed confocal microscopy of retinal flatmounts from *Tmem119*^{GFP/+} mice to determine where perivascular macrophages reside anatomically. Retinas were stained for CD31 to visualize vasculature and IBA1 to identify all macrophages. Microglia were defined as IBA1⁺GFP⁺ ramified cells (Fig 2A-D, orange arrow heads). Perivascular macrophages were identified as IBA1⁺GFP^{neg} cells along CD31⁺ vessels (white arrowheads). Hyalocytes were delineated as IBA1⁺GFP^{neg} non-ramified cells not on vessels (red arrowheads). Microglia were found in all vascular plexuses (Fig 2E) while perivascular macrophages and hyalocytes were only found in the superficial vascular plexus (Fig 2F-G). Next, we performed MotiQ morphometric analysis (16) on microglia (N=50 cells), perivascular macrophages (N=25 cells), and hyalocytes (N=25 cells) from 5-6 mice per group. We found that microglia demonstrated greater total area, spanned area (polygonal area connecting the outer points of the dendritic arbor), and tree length (sum of dendrites) compared to both perivascular macrophages and hyalocytes (Fig 2H-J). Additionally, hyalocytes were the least ramified while perivascular macrophages were intermediate and microglia demonstrated that greatest ramification index (Fig 2K).

Since the superficial vascular plexus contains arterioles and venules, while the intermediate and deep capillary plexuses are entirely capillaries, we next investigated if perivascular macrophages reside on arterioles or venules. Smooth muscle actin (SMA)

was used to identify arterioles (Fig 3A). Perivascular macrophages were found almost entirely on venules (Fig 3B-C). We next measured the diameter of vessels where perivascular macrophages dwell. We found that perivascular macrophages reside on post-capillary venules with an average diameter of 27.8 microns (range 11-51 microns, Fig 3D). Since post-capillary venules are the site of transendothelial migration of immune cells (12), and macrophage-endothelial crosstalk mediates immune cell tissue infiltration (11), we hypothesized that retinal perivascular macrophages may regulate immune cell infiltration into the retina.

To test this hypothesis, we sought to create a genetic mouse model to target perivascular macrophages. We used previously published retinal single-cell RNA-sequencing (scRNA-seq) data available on Spectacle (17, 18). We first identified 4 clusters of *Aif1*/IBA1⁺ tissue resident macrophages present in wild-type mouse retinas (Fig. 4A, Fig. S2A-B). We hypothesized that these clusters would contain microglia, hyalocytes, and perivascular macrophages. Three of four clusters were strongly positive for microglial markers *Tmem119* and *P2ry12*, and were thus named microglia (MG) 1, 2, and 3 (Fig. S2C-D). The fourth cluster, named non-microglia (non-MG) did not express *Tmem119* or *P2ry12* (Fig. S2C-D) but did express *Mrc1*/CD206 (Fig. S2E). Based on this fourth cluster's expression of *Mrc1*/CD206 (a marker of non-microglial tissue resident macrophages such as perivascular macrophages, Fig. 1), and lack of microglial markers *Tmem119* and *P2ry12*, we hypothesized that the non-MG cluster was enriched with perivascular macrophages. Differential gene expression analysis comparing MG1, MG2, and MG3 in aggregate vs. non-MG identified *PF4*/CXCL4 as a robustly expressed candidate marker of the non-MG cluster and perivascular macrophages (Fig. 4B-C).

To test the specificity of *PF4/CXCL4* for perivascular macrophages, we bred *Pf4^{Cre}* to *Rosa26^{CAG-LSL-ZsGreen1}* reporter mice (hereafter referred to as *Pf4-zsGreen*). We found that perivascular macrophages (white arrowheads) and vitreal hyalocytes (orange arrowheads) were 89% and 88% *zsGreen*⁺, respectively, compared to microglia which expressed *zsGreen* in 1% of cells (Fig 4D-E). CD169 staining was used to confirm that *zsGreen*⁺ cells away from vessels were vitreal hyalocytes and not microglia (Fig 4F-H). Additionally, we confirmed that both *zsGreen*⁺ perivascular macrophages and *zsGreen*⁺ hyalocytes co-stained with CD206 (Fig 4I-K), as expected from Fig 4B-C. These data demonstrate that *Pf4^{Cre}* mice effectively target perivascular macrophages and hyalocytes.

The above analysis did not quantify the many *zsGreen*⁺ cells observed on the optic nerve head. (Fig 4E). To further investigate these cells, we performed immunofluorescence of frozen section from *Pf4-zsGreen* mice. Frozen sections were stained for neurofilament to determine if these optic nerve head *zsGreen*⁺ cells were optic nerve head microglia. *zsGreen*⁺*IBA1*⁺*CD31*^{neg} cells (red arrowhead) in the vitreous side of the optic nerve head were identified as vitreal hyalocytes (Fig S2A-C). *zsGreen*⁺*IBA1*⁺*CD31*⁺ perivascular macrophages (white arrowhead) were also found at the optic nerve head (Fig S2A-C). *zsGreen*^{neg}*IBA1*⁺*Neurofilament*⁺ microglia (orange arrowhead) were detectable in the retina adjacent to the optic nerve head and in the optic nerve substance, but none were found at the optic nerve head (Fig S2A-D). These data suggest that optic nerve head *zsGreen*⁺ macrophages are a mixture of perivascular macrophages and vitreal hyalocytes.

To determine if brain perivascular macrophages also preferred venules to arterioles, we performed immunofluorescence imaging on brain frozen sections from *Pf4-*

zsGreen mice. Representative images are shown in Fig S4A-C. Perivascular macrophages were identified as CD206⁺IBA1⁺CD31^{adjacent}. Arterioles were discriminated from venules using SMA. Border-associated macrophages were delineated as CD206⁺IBA1⁺CD31^{neg} at the dural border of the brain. Microglia were defined as CD206^{neg}IBA1⁺. In the brain, perivascular macrophages were 93% *zsGreen*⁺ while microglia were only 7.2% *zsGreen*⁺ (Fig S4D), similar to retina. Unlike the retina, brain perivascular macrophages showed no preference for venules compared to arterioles (Fig S4E).

To infer perivascular macrophage function, we reanalyzed recently published scRNA-seq data from our laboratory (19, 20). This dataset included fluorescence-activated cell sorted CD45⁺ cells from wildtype eyes, *Ccr2*^{-/-} eyes, wildtype retina/choroid, and *Nr4a1*^{-/-} retina/choroid. Of note, no laser-treated samples from the original study were included in the reanalysis. From this integrated, reclustered mononuclear phagocyte subset, we identified three *Tmem119*⁺*P2ry12*⁺ microglia (Mg) clusters, *Gpnmb*⁺*Cst7*⁺ disease-associated microglia (DAM), *Ifit2*⁺*Ifit3*⁺ interferon microglia, two *Pf4*⁺*Mrc1*⁺ potential perivascular macrophage populations (Pf4-A and Pf4-B, red arrows), five *Aif1*⁺*C1qa*⁺*CD68*⁺ macrophage clusters, *Ly6c2*⁺*Ccr2*⁺ classical monocytes (C-Mono), two *Ace*⁺*Spn*⁺ non-classical monocyte subsets (NCM), three *Flt3*⁺ dendritic cell populations (DC), and *Fcer1a*⁺*Kit*⁺ mast cells (Fig 5A-B). The DAM population corresponded to previously published sub-retinal microglia (Fig S5A-B), which can be present at low numbers (~1-3%, Fig S5C) in young, wildtype mice (17, 21, 22). Compared to microglia, we noted that Pf4-A and Pf4-B expressed moderate levels of MHCII genes *H2-Ab1* and *H2-Eb1* (Fig 5B). Using multi-parameter flow cytometry gating as shown in Fig. 1A, we

found that both perivascular macrophage and hyalocytes expressed significantly greater MHCII than microglia (Fig 5C-D). Additionally, we stained *Tmem119*^{GFP/+} retina flatmounts for MHCII and found that perivascular macrophages were the predominant MHCII expressing cells in the retina (Fig 5E-F). Based upon these data, we suspected that either Pf4-A or Pf4-B were perivascular macrophages. We next performed differential expression (Table S1) followed by gene ontology (GO) enrichment analysis (Table S2). We found that Pf4-A was enriched for antigen presentation via MHCII (13.41 fold, $q < 0.01$), and chemotaxis of eosinophils (35.92 fold; genes = *Ccl2*, *Ccl4*, *Ccl7*, *Ccl12*, *Ccl24*; $q < 0.001$), lymphocytes (21.55 fold; genes = *Ccl2*, *Ccl3*, *Ccl4*, *Ccl7*, *Ccl12*, *Ccl24*, *Gas6*, *Gpr143*, *Ch25h*; $q < 0.001$), monocytes (16.76 fold; genes = *Ccl2*, *Ccl3*, *Ccl4*, *Ccl7*, *Ccl12*, *Ccl24*; $q < 0.001$), and neutrophils (11.70 fold; genes = *Cxcl1*, *Cxcl2*, *C5ar1*, *Ccl2*, *Ccl3*, *Ccl4*, *Ccl7*, *Ccl12*, *Ccl24*, *Pf4*; $q < 0.001$, Fig 5G-H). Similarly, Pf4-B demonstrated enrichment for chemotaxis of eosinophils (12.11 fold; genes = *Ccl2*, *Ccl7*, *Ccl8*, *Ccl24*; $q < 0.05$), lymphocytes (7.71 fold; genes = *Ccl2*, *Ccl6*, *Ccl7*, *Ccl8*, *Ccl9*, *Ccl24*, *Gas6*; $q < 0.01$), monocytes (8.93 fold, $q < 0.01$), and neutrophils (4.96 fold; genes = *Ccl2*, *Ccl6*, *Ccl7*, *Ccl8*, *Ccl9*, *Ccl24*, *Pf4*, *Pde4d*, *Vav3*; $q < 0.01$, Fig 5G-H). Based upon these data, Pf4⁺ macrophages are enriched for chemotaxis genes, supporting our hypothesis that retinal perivascular macrophages may regulate immune cell infiltration into the retina.

To initially test this hypothesis, we injected the chemokine CCL2, which is increased during DR (23), into the vitreous of *Tmem119*^{GFP/+} mice (Fig 6A). CCL2 binds the CCR2 receptor and recruits classical Ly6C⁺ monocytes to tissue. To our surprise, despite injecting CCL2 into the peripheral vitreous, the majority of infiltrating Ly6C⁺ cells were detected near the optic nerve (Fig 6B-F). We quantitated the distance of each

microglia, hyalocyte, perivascular macrophages, and Ly6C⁺ cell from the optic nerve. We found a significant correlation between the distributions of Ly6C⁺ cells and perivascular macrophages ($p < 0.05$). We repeated the CCL2 study in *Pf4-zsGreen* mice. We found that intravascular Ly6C⁺ cells were detectable near zsGreen⁺ perivascular macrophages (Fig 6G-H). Importantly, Ly6C⁺ cells did not express zsGreen, suggesting that classical monocytes and bone marrow precursors do not express *Pf4* immediately after tissue infiltration.

Next, we generated *Pf4^{Cre} :: Rosa26^{CAG-LSL-DTR/+}* (*Pf4-DTR*) mice to deplete perivascular macrophages with diphtheria toxin (DT) injections. Ten-twelve week-old *Pf4-DTR* mice were treated with vehicle PBS or DT for 4 days. Importantly, 4 days of DT treatment had no effect on animal health. On Day 5, retinal flatmounts were stained for CD31, IBA1, and DTR (DT receptor). We found that DT-treated mice demonstrated a 32% reduction in DTR⁺ retinal perivascular macrophages ($p < 0.01$) with no change in DTR⁺ hyalocytes (Fig 7A-C) or retinal microglia (Fig S6). The discrepancy between 32% perivascular macrophage ablation in *Pf4-DTR* mice compared to 89% targeting with *Pf4-zsGreen* (Fig 4F) is likely due to the low dose DT (200 ng), or the fact that the same promoter can have differential efficiency even between Rosa26 reporter lines (24).

Next, we repeated the above study and performed fluorescein angiography (FA) followed by systemic perfusion with fluorescently labeled dextran to test vascular permeability of both albumin-bound (66 kDa) fluorescein and 10 kDa dextran. In PBS-treated *Pf4-DTR* mice, 7 of 9 eyes showed completely normal vascular permeability in both assays (Fig S7A). In 2 of 9 eyes, vascular permeability was increased predominantly in the 10 kDa dextran assay with marginal FA findings (Fig S7B). In DT-treated *Pf4-DTR*

mice, 6 of 9 eyes were normal (Fig S7C) while 3 of 9 eyes showed increased vascular permeability (Fig S7D). There was no significant difference between PBS- (22%) and DT- (33%) treated eyes ($p=0.28$).

Next, tested the role of perivascular macrophages in immune cell infiltration by repeating our PBS and DT protocol followed by intravitreal CCL2 injections on Day 4 and sacrificed mice on Day 5 in *Pf4-DTR* mice. DT-mediated ablation of perivascular macrophages decreased CCL2-driven Ly6C⁺ cell infiltration by 75.8% ($p<0.01$, Fig 7D-H). These data suggest that perivascular macrophages are necessary for acute CCL2-driven neuroinflammation.

Finally, we repeated the above study and additionally performed both FA and 10 kDa dextran perfusion assays. FA showed vascular hyperpermeability around the optic nerve head in both PBS- and DT-treated eyes that received intravitreal CCL2 injections (Fig S8A-B). The number of Ly6C⁺ cells was significantly reduced in DT-treated eyes while the 10 kDa dextran leakage was reduced to similar or less degrees (Fig S8C-D). Optical coherence tomography (OCT) showed dramatically reduced immune cell extravasation near the optic nerve (Fig S8E-F). Total vascular leakage showed a trend toward a reduction in DT-treated eyes (Fig S8G). Since immune cell infiltration will secondarily affect vascular permeability, this under-powered study suggests that perivascular macrophage ablation primarily affects immune cell extravasation but further investigation is warranted.

Discussion

In this report, we comprehensively characterized perivascular macrophages in the retina to determine their function. We found that retinal perivascular macrophages reside on 20-40 micron post-capillary venules (Fig 2-3), are targetable with *Pf4^{Cre}* mice (Fig 4), and express a pro-chemotactic transcriptome (Fig 5). Based upon these data, we hypothesized that perivascular macrophages are necessary for immune cell infiltration during acute neuroinflammation. This hypothesis is supported by prior reports that immune cell transendothelial migration occurs at post-capillary venules in multiple organ systems (12) including the retina (25), macrophage-endothelial crosstalk can orchestrate immune cell infiltration (11), and *Pf4/CXCL4* regulates immune cell recruitment (26). We modeled neuroinflammation with a single CCL2 intravitreal injection and found that perivascular macrophages were associated with Ly6C⁺ cells (Fig 6) and perivascular macrophage depletion significantly reduced Ly6C⁺ cell recruitment (Fig 7). These data suggest that perivascular macrophages are key members of the BRB and orchestrate immune cell recruitment during neuroinflammation.

Although retinal perivascular macrophages are extremely understudied, perivascular macrophages have been investigated in other neural tissues. In the brain, perivascular macrophages are similarly CD206⁺ and reside within the vascular sheath (3). Their functions include the regulation of immune cell chemotaxis and vascular permeability (3, 10, 27), in partial agreement with our studies. We also find that retinal perivascular macrophages regulate immune cell infiltration (Fig 7). However, there was no significant effect of retinal perivascular macrophage ablation at steady-state on vascular permeability (Fig S7). After CCL2 intravitreal injection, perivascular macrophage ablation showed a trend toward less vascular permeability but the effect size was equal or less

than immune cell chemotaxis. Since immune cell infiltration can secondary affect vascular permeability, our data support a more substantial impact of perivascular macrophages on chemotaxis than permeability. This conclusion is supported by our scRNA-seq data which shows increased chemotaxis genes but no change in extracellular matrix or permeability genes. Nevertheless, these studies are under-powered and warrant further investigation.

Additionally, brain perivascular macrophages express MHCII and are capable of antigen presentation (28, 29), also in agreement with our findings. In partial alignment with our findings, brain perivascular macrophages reside on venules and arterioles, but not capillaries (9). We replicated this data in the brain and found no arteriolar or venular preference (Fig S4), but a clear preference for venules in the eye (Fig 3). These interesting differences may be related to vessel size and warrant further investigation. Furthermore, perivascular macrophages in the brain are derived from meningeal macrophages and demonstrate heterogeneity (9, 30), two important areas of future investigation in the retina. We similarly find heterogeneity in the expression of MHCII in retinal perivascular macrophages. In the spinal cord, perivascular macrophages also express MHCII heterogeneously and regulate vascular permeability through extracellular matrix protein levels in a model of amyotrophic lateral sclerosis (31). Finally, both brain and dorsal root ganglion perivascular macrophages express CD163 (28, 32). CD163⁺ dorsal root ganglion perivascular macrophages differentially express *Pf4* and *Ccl24*, similar to the retina, and regulate endothelial permeability like the brain (32). These data demonstrate potential conserved functions across tissues between central nervous system perivascular macrophages in terms of antigen presentation, vascular permeability, and immune cell chemotaxis.

Since retinal perivascular macrophages are necessary for CCL2-driven immune cell infiltration, they may play an important role in the pathophysiology of DR. In murine DR models, retinal *Ccl2* expression is up-regulated; further, *Ccl2*^{-/-} and *Ccr2*^{-/-} mice both show reduced immune cell leukostasis and infiltration, decreased vascular permeability, and less endothelial cell death (33, 34). These data demonstrate the pathogenic role of classical monocytes and classical monocyte-derived macrophages in DR progression and breakdown of the BRB during murine DR. In agreement between mice and humans, BRB disruption is associated with more advanced DR stage (1), and CCL2 levels are increased in DR patients and correlate with diabetic macular edema (23), a marked source of vision loss in patients with DR. Furthermore, intravitreal steroids are an effective treatment for both diabetic macular edema and regression of DR stage in clinical trials (35, 36), demonstrating the importance of inflammation and BRB breakdown in human DR. Finally, imaging of macrophage-like cells at the vitreoretinal interface in patients with DR shows that the number of these cells increases with advanced DR stage, diabetic macular edema, and ischemia (37–41). Macrophage-like cells at the vitreoretinal interface have the potential to include microglia, perivascular macrophages, vitreal hyalocytes, and recruited inflammatory cells (13). Together, these data suggest that BRB breakdown leads to inflammatory cell recruitment, resulting in diabetic macular edema and DR stage progression, which includes proliferative DR (PDR) with neovascularization. In agreement, scRNA-seq from human PDR membranes demonstrates that non-microglial macrophages are present and express high amounts of *VEGFA* (42). Thus, perivascular macrophages are potential key pathogenic cells in both BRB breakdown and immune cell infiltration, which are central processes in the pathophysiology of DR.

Retinal perivascular macrophages may also play important roles in the pathophysiology of non-infectious intraocular inflammation or uveitis. Similar to DR, retina-involving uveitis is a disease that includes breakdown of the BRB. In mice, uveitis is modeled using the experimental autoimmune uveitis (EAU) model. In EAU, mice are immunized with interphotoreceptor retinoid-binding protein (IRBP). IRBP is expressed by photoreceptor outer segments and immunization targets the immune response to photoreceptors (43). For initiation of EAU to occur, both MHCII-dependent antigen presentation and retinal macrophages are necessary (43, 44). In addition, early immune cell infiltration during EAU occurs from large vessels in the superficial vascular plexus (45). Furthermore, the early events of EAU include leukocyte adhesion to postcapillary venules, breakdown of the BRB, and finally immune cell infiltration into the retinal parenchyma (46). Since perivascular macrophages are the predominant MHCII⁺ retinal macrophages, are found in the superficial vascular plexus, and are predominantly associated with venules, future investigations into the role of perivascular macrophages in EAU are warranted.

This study has several limitations. First, our *Pf4^{Cre}* model also targets hyalocytes. However, DT-driven ablation did not reduce hyalocyte levels. This is likely either because hyalocytes exist within the BRB barrier or because of the high density of hyalocytes and perivascular macrophages that exist over the optic nerve head. This area was too dense to definitively discriminate between hyalocytes and perivascular macrophages with high certainty. Thus, we cannot exclude that our reduction in immune cell chemotaxis after CCL2 intravitreal injections is not due to hyalocyte depletion. Second, we did not investigate the effects of perivascular macrophage depletion on endothelial cells. Since

perivascular macrophages are only present on large venules in the eye, a bulk RNA-seq approach of sorted endothelial cells would likely not yield marked differences due to the many capillary endothelial cells without perivascular macrophage contact. To investigate how perivascular macrophages influence endothelial cells, a scRNA-seq or spatial transcriptomics approach would be necessary to understand how large post-capillary venule endothelial cells change after perivascular macrophage ablation, which is beyond the scope of this current manuscript. Third, we also did not investigate how perivascular macrophage ablation affects extracellular matrix proteins like collagen IV or laminin, which have been shown to be regulated by perivascular macrophages in amyotrophic lateral sclerosis (31). In the Adachi *et al* study, these extracellular matrix proteins were affected by perivascular macrophage ablation that occurred over 6 weeks. Therefore, more chronic ablation is likely necessary to uncover these changes and is an area of future investigation. Finally, *Pf4*/CXCL4 is a chemokine expressed in other cells external to the retina. Although *Pf4* was not expressed in extravasating Ly6C⁺ monocytes (Fig 6H), we cannot exclude an effect of reduced CXCL4 expression in stromal or non-monocyte hematopoietic bone marrow or blood cells prior to ocular infiltration.

In summary, retinal perivascular macrophages express MHCII, are located on post-capillary venules, and are targetable with *Pf4*^{Cre} mice. Furthermore, *Pf4*⁺ macrophages express a pro-chemotactic transcriptome, correlate with immune cell chemotaxis, and are necessary for Ly6C⁺ immune cell infiltration after intravitreal CCL2 injection. These data suggest that perivascular macrophages are key members of the blood-retina barrier that regulate immune cell transendothelial migration and may play important roles during DR and uveitis pathophysiology.

Methods

Sex as a biological variable

All studies were carried out on mixed sex populations with a minimum of 2 animals per sex per group. All data were investigated for sex-specific effects and none were found.

Animals

Wildtype C57BL/6J (#000664), *Tmem119^{GFP}* (#031823), *Rosa26^{CAG-LSL-ZsGreen1}* (#007906), *Rosa26^{CAG-LSL-DTR}* (#007900), and *Pf4^{Cre}* (#008535) mice were purchased from Jackson Labs (Bar Harbor, ME). Wildtype C57BL/6J were bred and maintained within a pathogen-free barrier environment at the Center for Comparative Medicine at Northwestern University. *Tmem119^{GFP}* mice were crossed with wildtype mice to generate *Tmem119^{GFP/+}* mice for experiments. *Pf4^{Cre}* mice were bred with *Rosa26^{CAG-LSL-ZsGreen1}* and *Rosa26^{CAG-LSL-DTR}* mice to generate *Pf4^{Cre} :: Rosa26^{ZsGreen/+}* (*Pf4-zsGreen*) and *Pf4^{Cre} :: Rosa26^{CAG-LSL-DTR/+}* (*Pf4-DTR*) mice for experiments, respectively. Genotyping was performed by Transnetyx (Cordova, TN) to confirm the absence of the RD8 allele (*Crb1⁻*). All studies adhered to the ARVO Statement for Animal Use in Ophthalmic and Vision Research and received approval from the Northwestern University Institutional Animal Care and Use Committee. Unless otherwise specified, all experiments were carried out on 10-12 week old mice.

Flow cytometry of mouse retina

Following enucleation, eyes were transported in HBSS (14025076, Gibco, Carlsbad, CA) and dissected under a microscope to isolate retina. Retina only samples were digested and processed identically to our previously published flow cytometry

procedure with the exception that no mechanical digestion was performed (47). A single cell suspension was prepared and then stained with immune cell markers (Table S1). All experiments were analyzed on a FACSymphony A5-Laser Analyzer (Becton Dickinson, CA, USA); data were analyzed using FlowJo version 10 (FlowJo, Ashland, OR).

Immunofluorescence imaging of retinal flatmounts

After mice were sacrificed, eyes were enucleated and fixed in 4% paraformaldehyde (#15713-S; Electron Microscopy Sciences, Hatfield, PA, USA) for 1 hour at room temperature. Retinas were isolated in 1X TBS (Tris-buffered saline) and stored in TBS + 5% Donkey Serum (#S30, Sigma-Aldrich, St. Louis, MO) + 2.5% bovine serum albumin (A2153, Sigma) + 0.5% Triton X-100 (X100; Sigma) overnight at 4°C. Primary incubations were performed overnight at 4°C (Table S1). Next, retinas were washed with TBS-T (TBS with 0.5% Tween-20, #00777; Amresco, Solon, OH, USA) 5 times and incubated with secondary antibodies overnight at 4°C (Table S1). Retinas were then washed with TBS-T and mounted on HistoBond microscope slides (#16004–406, VWR; Batavia, IL, USA) with Immu-Mount (#9990402; ThermoFisher, Carlsbad, CA, USA). Imaging was performed on a Nikon W1 Dual CAM Spinning Disk Microscope using Nikon NIS Elements software. The approximate distances between vascular plexuses were 8-11 microns between superficial and intermediate, and 8-12 microns between intermediate and deep.

Immunofluorescence imaging of frozen sections

Eyes were processed identically to our previously published manuscript (13). For frozen brain sections, mice were perfused with ice cold HBSS, brains were extracted from the skull, and cut along the median longitudinal fissure. Brains were fixed in 4%

paraformaldehyde at room temperature for 2 hours. Brains were washed in PBS, 10%, 20% and 30% sucrose identically to eyes. Next, the brains were placed in a 25 mm x 20 mm x 5 mm vinyl specimen mold (4557, Sakura, CA, USA) with the sliced side on the bottom of the mold and embedded in optical cutting temperature compound (#23-730-571, Fisher Healthcare, Pittsburgh, PA). The samples were frozen at -80°C and cut into 8-micron sections with a cryostat. Eye and brain sections were stained identically. Slides were washed in PBS for 10 minutes, blocked for 1 hour at room temperature in 5% donkey serum, and then stained identically to retinal flatmounts. Immunofluorescence was performed on a Nikon Ti2 Widefield using Nikon NIS elements software.

MotiQ Analysis

We selected 50 microglia, 25 perivascular macrophages, and 25 hyalocytes from the superficial vascular plexus (N=5-6 mice) for MotiQ analysis, as previously described (16). We performed total area, spanned area, tree length, and ramification index.

Single-cell RNA-sequencing analysis

We analyzed single-cell RNA-sequencing (scRNA-seq) previously published by O'Koren et al using Spectacle (singlecell-eye.org) (17, 18). We analyzed our own prior scRNA-seq data using Seurat v4 (19, 20, 48). This analysis used only RNA-seq data from control no laser eyes or control no laser choroid/retina from wildtype, *Ccr2*^{-/-}, and *Nr4a1*^{-/-} mice. Quality control metrics were identical to our prior reports (19, 20). Data were independently normalized, scaled, and then integrated using reciprocal principal component analysis (49). Clustering was performed using the standard workflow with 22 principal components and 0.4 resolution. A mononuclear phagocyte subset was created, rescaled, renormalized, and reclustered using 17 principal components and 0.7

resolution. The Wilcoxon Rank Sum test was used for differential expression using the FindAllMarkers function within Seurat (>10% of cells, log2FC > 0.59 (1.5-fold) between the cluster of interest and all other cells). We chose the 1.5-fold cutoff so that were enough differentially expressed genes in each cluster for gene ontology (GO) enrichment analysis. GO enrichment analysis was performed on upregulated genes >1.5 fold with adjusted p value <0.01. GO enrichment was performed using Gorilla (50), with a background of genes expressed in >5% of mononuclear phagocytes. Selected GO terms are shown in Figure 5E; all GO terms are in Supplemental Table 3. The DotPlot function was used to visualize genes that were included in selected GO terms. Specific code is available upon reasonable request.

Intravitreal injections

Mice were anesthetized, eyes were dilated, and pain prophylaxis was provided as previously described (51). Intravitreal injections were performed identically to our previously report using 1 ng of CCL2 in 1 µl of sterile PBS (13). Retinal flatmount immunofluorescence imaging or flow cytometry was performed 18 hours after intravitreal injections.

Diphtheria toxin administration

Intraperitoneal injections of sterile PBS vehicle control or 200ng of diphtheria toxin (#322326-1MG, MilliporeSigma, Burlington, MA) in 0.1 mL of PBS were administered for 4 consecutive days. Intravitreal injections were given on Day 4. Mice were sacrificed on Day 5 for immunofluorescence of retinal flatmounts or flow cytometry.

Optical Coherence Tomography and Vascular Permeability Assays

Mice were anesthetized, eyes were dilated, and pain prophylaxis was provided as previously described (51). Mice were given a single intraperitoneal injection of 0.05 mL of AK-FLUOR 25% (sodium fluorescein, 250 mg/ml) for fluorescein angiography. Mice were next positioned at the Spectralis OCT2 system (Heidelberg Engineering, Heidelberg, Germany) for fluorescein angiography and OCT imaging. A contact lens was placed on the surface of the eye (Cantor and Nissel, 3.2 mm diameter, 1.7 mm base curve, #90,642). Late phase fluorescein angiography images were taken at 5 minutes post-fluorescein injection with 100 frame averaging for high resolution. High resolution OCT images at the optic nerve were taken averaging 100 frames. Mice were next given a retro-orbital injection of 10 kDa Dextran (Invitrogen, D22914, 5 mg/ml), as previously described (52). Five minutes post retro-orbital injection, eyes were processed for confocal microscopy as described above. Total leakage was calculated in FIJI by using the ROI manager function to delineate the leakage area and measure both area and mean intensity. The area was multiplied by mean intensity for total leakage per eye.

Statistical analysis

For flow cytometry studies, CD206 MFI, CD169 MFI, MHCII MFI and cell counts were compared using repeated measures one-way ANOVA followed by Tukey's multiple comparisons test. For immunofluorescence studies, macrophage subset counts were compared using repeated measures one-way ANOVA followed by Tukey's multiple comparisons test or paired two-tailed t-test. For MotiQ analysis, one-way ANOVA followed by Tukey's multiple comparisons test was performed. Overlap between perivascular macrophages and Ly6C⁺ cells were compared using a transformation of the Kolmogorov-Smirnov test. Percent depletion of cells was compared using two-way ANOVA followed

by Sidak's multiple comparisons test. Ly6C⁺ monocyte density was compared using the Mann-Whitney test because the distribution was non-parametric on the Shapiro-Wilk test. A p-value <0.05 was considered statistically significant. All data are presented as mean ± standard error mean.

Study Approval

All studies were performed in accordance with protocols approved by the Northwestern University Institutional Animal Care and Use Committee.

Data Availability

Raw scRNA-seq data is already available on the GEO omnibus (GSE239941 and GSE222094). All other data will be available upon reasonable request to the corresponding author. All data values in graphs are available in the supporting data values (Raw Graph Data) excel sheet.

Author contributions

Jacob K Sterling's roles included conceptualization, formal analysis, data curation, investigation, methodology, visualization, and writing of the original draft. Amrita Rajesh's role was investigation, formal analysis, methodology, and writing review and editing. Jacob K Sterling was chosen as the first author, despite equal overall contribution with Amrita Rajesh, due to his role in conceptualization and writing of the original draft. Steven Droho's roles included data curation, investigation, methodology, and writing review and editing. Joyce Gong's roles included investigation and writing review and editing. Andrew Wang's roles included data curation, investigation, and writing review and editing. Andrew Voigt's roles included data curation, formal analysis, and writing review and editing. C.

Elysse Brookin's roles included investigation and writing review and editing. Jeremy A Lavine's roles were conceptualization, data curation, formal analysis, funding acquisition, investigation, methodology, project administration, supervision, visualization, and writing the original draft as well as editing and review.

Acknowledgements

This study was supported by an Unrestricted Departmental Grant from Research to Prevent Blindness. JKS was supported by the NEI Ruth L. Kirschstein Individual Predoctoral NRSA Fellowship F30 EY032339. JAL was supported by NIH grant K08 EY030923, R01 EY034486, and the Research to Prevent Blindness Sybil B. Harrington Career Development Award for Macular Degeneration. Imaging work was performed at the Northwestern University Center for Advanced Microscopy generously supported by CCSG P30 CA060553 awarded to the Robert H Lurie Comprehensive Cancer Center. Flow cytometry was performed at the Northwestern University - Flow Cytometry Core Facility supported by Cancer Center Support Grant (NCI CA060553). No funding body had any role in the design of the study, collection, analysis, interpretation of data, or in writing the manuscript. JAL is a consultant for Line 6 Biotechnology and Genentech. JAL received research grant support from Therini Bio. No company body had any role in the design of the study, collection, analysis, interpretation of data, or in writing the manuscript. The authors have no additional financial interests.

References

1. Ehlers JP, et al. Quantitative Ultra-Widefield Angiography and Diabetic Retinopathy Severity: An Assessment of Panretinal Leakage Index, Ischemic Index and Microaneurysm Count. *Ophthalmology*. 2019;126(11):1527–1532.
2. Pecun PE, et al. Peripheral Findings and Retinal Vascular Leakage on Ultra-Widefield Fluorescein Angiography in Patients with Uveitis. *Ophthalmol Retin*. 2017;1(5):428–434.
3. Faraco G, et al. Perivascular macrophages mediate the neurovascular and cognitive dysfunction associated with hypertension. *J Clin Invest*. 2016;126(12):4674–4689.
4. Wolter JR. Perivascular Glia of the Blood Vessels of the Human Retina*. *Am J Ophthalmol*. 1957;44(6):766–773.
5. Mendes-Jorge L, et al. Scavenger function of resident autofluorescent perivascular macrophages and their contribution to the maintenance of the blood-retinal barrier. *Invest Ophthalmol Vis Sci*. 2009;50(12):5997–6005.
6. Chaurasia SS, et al. The NLRP3 Inflammasome May Contribute to Pathologic Neovascularization in the Advanced Stages of Diabetic Retinopathy. *Sci Rep*. 2018;8(1):2847.
7. Roubeyx C, et al. Mo-derived perivascular macrophage recruitment protects against endothelial cell death in retinal vein occlusion. *Journal of Neuroinflammation*. 2019;1–9.
8. Dabouz R, et al. An allosteric interleukin-1 receptor modulator mitigates inflammation and photoreceptor toxicity in a model of retinal degeneration. *J Neuroinflammation*. 2020;17(1):359.
9. Masuda T, et al. Specification of CNS macrophage subsets occurs postnatally in defined niches. *Nature*. 2022;604(7907):740–748.
10. Park L, et al. Brain Perivascular Macrophages Initiate the Neurovascular Dysfunction of Alzheimer A β Peptides. *Circulation Research*. 2017;121(3):258–269.
11. Ren X, et al. Macrophage-endothelial cell crosstalk orchestrates neutrophil recruitment in inflamed mucosa. *J Clin Invest*. 2023;133(15):e170733.
12. Muller WA. Transendothelial migration: unifying principles from the endothelial perspective. *Immunol Rev*. 2016;273(1):61–75.
13. Rajesh A, Droho S, Lavine JA. Macrophages in close proximity to the vitreoretinal interface are potential biomarkers of inflammation during retinal vascular disease. *J Neuroinflamm*. 2022;19(1):203.

14. Kaiser T, Feng G. Tmem119-EGFP and Tmem119-CreERT2 Transgenic Mice for Labeling and Manipulating Microglia. *eNeuro*. 2019;6(4):1–18.
15. Vagaja NN, et al. Changes in Murine Hyalocytes Are Valuable Early Indicators of Ocular Disease. *Invest Ophthalmol Vis Sci*. 2012;53(3):1445–7.
16. Hansen JN, et al. MotiQ: an open-source toolbox to quantify the cell motility and morphology of microglia. *Mol Biol Cell*. 2022;33(11):ar99.
17. O’Koren EG, et al. Microglial Function Is Distinct in Different Anatomical Locations during Retinal Homeostasis and Degeneration. *Immunity*. 2019;1–23.
18. Voigt AP, et al. Spectacle: An interactive resource for ocular single-cell RNA sequencing data analysis. *Exp Eye Res*. 2020;200:108204.
19. Droho S, et al. NR4A1 deletion promotes pro-angiogenic polarization of macrophages derived from classical monocytes in a mouse model of neovascular age-related macular degeneration. *J Neuroinflammation*. 2023;20(1):238.
20. Droho S, et al. CD11c+ macrophages are pro-angiogenic and necessary for experimental choroidal neovascularization. *JCI Insight*. 2023;8(7):e168142.
21. Yu C, et al. Microglia at sites of atrophy restrict the progression of retinal degeneration via galectin-3 and Trem2. *J Exp Med*. 2024;221(3):e20231011.
22. Karg MM, et al. Microglia preserve visual function in the aging retina by supporting retinal pigment epithelial health. *Immun Ageing*. 2023;20(1):53.
23. Wu J, et al. Aqueous Humor Mediator and Cytokine Aberrations in Diabetic Retinopathy and Diabetic Macular Edema: A Systematic Review and Meta-Analysis. *Dis Markers*. 2019;2019:6928524.
24. Bedolla AM, et al. A comparative evaluation of the strengths and potential caveats of the microglial inducible CreER mouse models. *Cell Rep*. 2024;43(1):113660.
25. Joseph A, et al. Label-free imaging of immune cell dynamics in the living retina using adaptive optics. *Elife*. 2020;9:365–14.
26. Gray AL, et al. Chemokine CXCL4 interactions with extracellular matrix proteoglycans mediate widespread immune cell recruitment independent of chemokine receptors. *Cell Reports*. 2023;42(1):111930.
27. Ineichen BV, et al. Perivascular spaces and their role in neuroinflammation. *Neuron*. 2022;110(21):3566–3581.

28. Swanson MEV, et al. Quantitative immunohistochemical analysis of myeloid cell marker expression in human cortex captures microglia heterogeneity with anatomical context. *Nature Publishing Group*. 2020;1–18.
29. Goddery EN, et al. Microglia and Perivascular Macrophages Act as Antigen Presenting Cells to Promote CD8 T Cell Infiltration of the Brain. *Front Immunol*. 2021;12:726421.
30. Siret C, et al. Deciphering the heterogeneity of the Lyve1+ perivascular macrophages in the mouse brain. *Nat Commun*. 2022;13(1):7366.
31. Adachi K, et al. Depletion of perivascular macrophages delays ALS disease progression by ameliorating blood-spinal cord barrier impairment in SOD1G93A mice. *Front Cell Neurosci*. 2023;17:1291673.
32. Lund H, et al. CD163+ macrophages monitor enhanced permeability at the blood–dorsal root ganglion barrier. *J Exp Med*. 2023;221(2):e20230675.
33. Rangasamy S, et al. Chemokine Mediated Monocyte Trafficking into the Retina: Role of Inflammation in Alteration of the Blood-Retinal Barrier in Diabetic Retinopathy. *PLoS ONE*. 2014;9(10):e108508-10.
34. Saadane A, et al. CCR2-positive monocytes contribute to the pathogenesis of early diabetic retinopathy in mice. *Diabetologia*. 2023;66(3):590–602.
35. Iglicki M, et al. Progression of diabetic retinopathy severity after treatment with dexamethasone implant: a 24-month cohort study the ‘DR-Pro-DEX Study.’ *Acta Diabetol*. 2018;55(6):541–547.
36. Boyer DS, et al. Three-Year, Randomized, Sham-Controlled Trial of Dexamethasone Intravitreal Implant in Patients with Diabetic Macular Edema. *Ophthalmology*. 2014;121(10):1904–1914.
37. Zhang NT, et al. Macrophage-like Cells Are Increased in Patients with Vision-Threatening Diabetic Retinopathy and Correlate with Macular Edema. *Diagnostics*. 2022;12(11):2793.
38. Ong JX, et al. Macrophage-Like Cell Density Is Increased in Proliferative Diabetic Retinopathy Characterized by Optical Coherence Tomography Angiography. *Invest Ophthalmol Vis Sci*. 2021;62(10):2–2.
39. Bisen JB, et al. Association between macrophage-like cell density and ischemia metrics in diabetic eyes. *Exp Eye Res*. 2023;237:109703.
40. Wang W, et al. Proliferative diabetic retinopathy and diabetic macular edema are two factors that increase macrophage-like cell density characterized by en face optical coherence tomography. *Bmc Ophthalmol*. 2023;23(1):46.

41. Wang Z, et al. Elevated number and density of macrophage-like cell as a novel inflammation biomarker in diabetic macular edema. *Sci Rep-uk*. 2023;13(1):5320.
42. Corano-Scheri K, et al. Single cell transcriptomic analysis of proliferative diabetic retinopathy fibrovascular membranes reveals AEBP1 as fibrogenesis modulator. *JCI Insight*. 2023;8(23). <https://doi.org/10.1172/jci.insight.172062>.
43. Okunuki Y, et al. Retinal microglia initiate neuroinflammation in ocular autoimmunity. *Proc Natl Acad Sci*. 2019;116(20):9989–9998.
44. Rao NA, et al. Suppression of experimental uveitis in rats by anti-I-A antibodies. *Investig Ophthalmol Vis Sci*. 1989;30(11):2348–55.
45. Gullapalli VK, et al. Hematopoietically derived retinal perivascular microglia initiate uveoretinitis in experimental autoimmune uveitis. *Graefe's Arch Clin Exp Ophthalmol*. 2000;238(4):319–325.
46. Xu H, et al. Leukocyte Trafficking in Experimental Autoimmune Uveitis: Breakdown of Blood–Retinal Barrier and Upregulation of Cellular Adhesion Molecules. *Investig Ophthalmology Vis Sci*. 2003;44(1):226.
47. Droho S, Cuda CM, Lavine JA. Digestion of Whole Mouse Eyes for Multi-Parameter Flow Cytometric Analysis of Mononuclear Phagocytes. *J Vis Exp*. 2020;(160):1–20.
48. Hao Y, et al. Integrated analysis of multimodal single-cell data. *Cell*. 2021;184(13):3573–3587.e29.
49. Stuart T, et al. Comprehensive Integration of Single-Cell Data. *Cell*. 2019;177(7):1888–1902.e21.
50. Eden E, et al. GOrilla: a tool for discovery and visualization of enriched GO terms in ranked gene lists. *BMC Bioinformatics*. 2009;10(1):25–7.
51. Droho S, et al. Monocyte-Derived Macrophages Are Necessary for Beta-Adrenergic Receptor-Driven Choroidal Neovascularization Inhibition. *Invest Ophth Vis Sci*. 2019;60(15):5059–5069.
52. Bhakuni T, et al. FOXC1 regulates endothelial CD98 (LAT1/4F2hc) expression in retinal angiogenesis and blood-retina barrier formation. *Nat Commun*. 2024;15(1):4097.

Figures

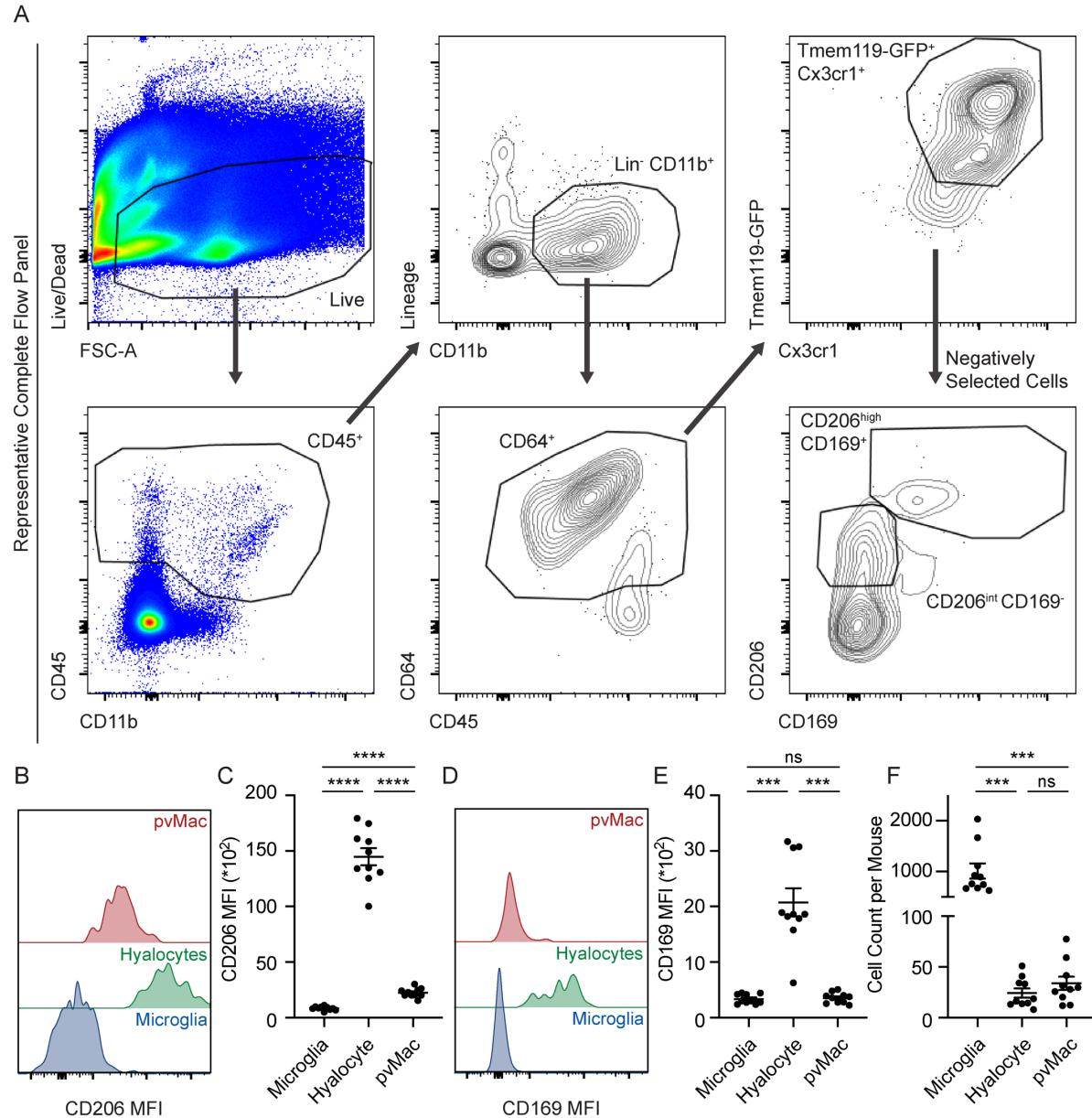


Figure 1. Flow cytometry identification of retinal macrophage heterogeneity. A: Flow cytometry gating strategy. Top left panel: Live cells were identified from singlets. Bottom left panel: CD45⁺ cells were identified from Live, Singlet cells. Top middle panel: Lineage (CD4, CD8 [T cells], B220 [B cells], Ly6G [neutrophils], NK1.1 [NK cells], SiglecF [eosinophils]) vs CD11b plot to gate forward CD11b⁺Lin^{neg} mononuclear phagocytes. Bottom middle panel: CD64⁺ macrophages were identified. Top right panel: Tmem119^{GFP} vs Cx3cr1 plot to delineate Cx3cr1^{high}Tmem119^{GFP} microglia. Bottom right panel: Not tmem119 were plotted on CD206 vs CD169 plot to identify CD206^{high}CD169⁺ hyalocytes and CD206^{int}CD169^{neg} perivascular macrophages. B: Modal frequency histogram for CD206 expression (MFI = mean fluorescence intensity). C: Hyalocytes express the most CD206 while perivascular macrophages (pvMac) express intermediate CD206 levels. D: Modal frequency histogram for CD169 expression. E: Hyalocytes express the most CD169 while pvMac express low CD169 levels. F: Microglia are the most abundant retinal macrophages, followed by perivascular macrophages, and hyalocytes. Data were analyzed by repeated measures one-way ANOVA followed by Tukey's multiple comparisons test: ** p<0.01, *** p<0.001, **** p<0.0001. N=10 per group.

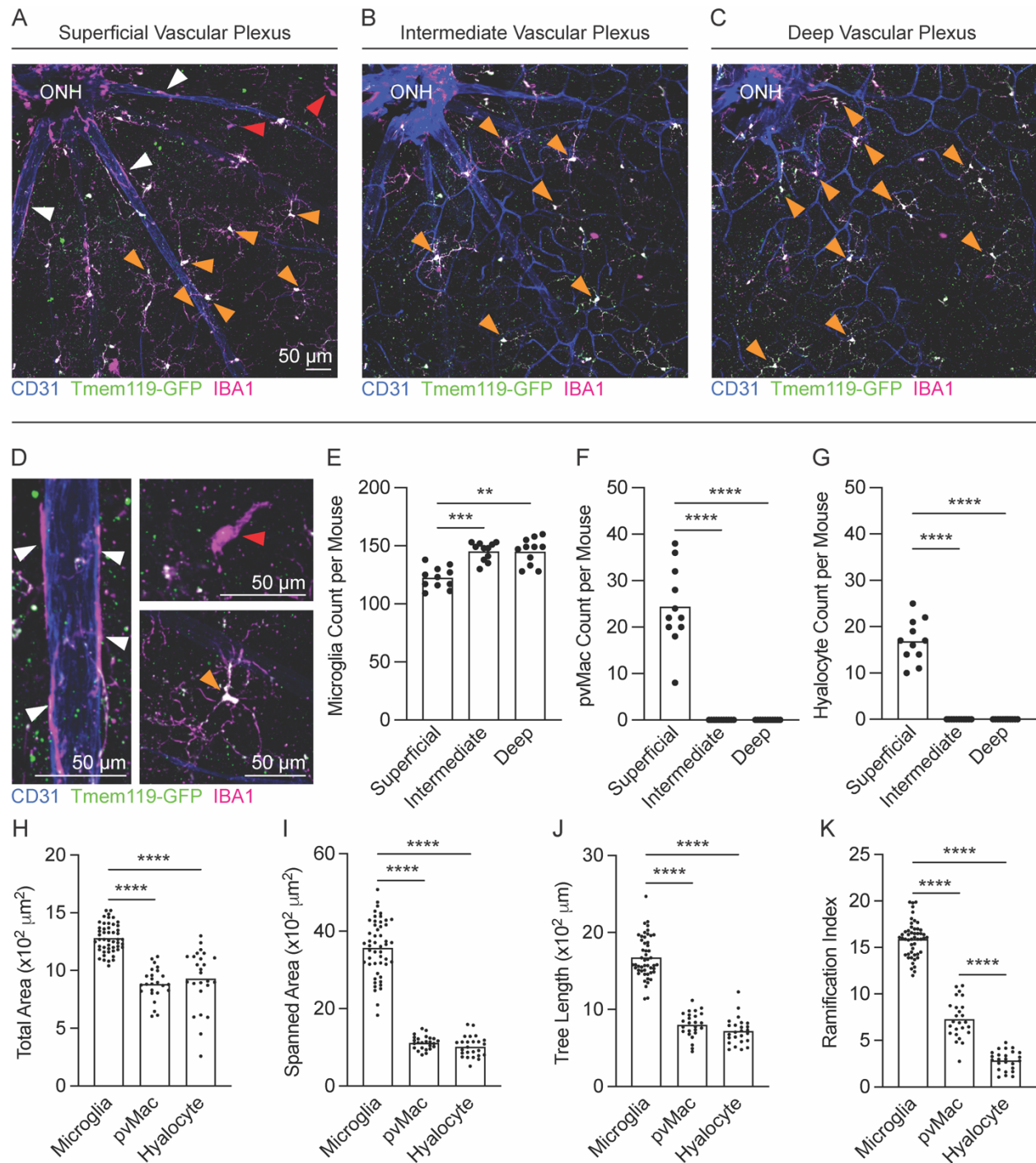


Figure 2. Perivascular macrophages only reside in the superficial vascular plexus. A-C: In the representative images of superficial (A), intermediate (B), and deep (C) vascular plexuses, white arrows identify perivascular macrophages (pvMac), orange arrows show microglia, and red arrows highlight hyalocytes. D: Zoomed in representative image of each cell type. E-G: Counts of microglia (E), pvMac (F), and hyalocytes (G) in each vascular plexus. Microglia are in all 3 plexuses, while perivascular macrophages and hyalocytes are only found in the superficial vascular plexus. Data were analyzed by repeated measures ANOVA followed by Tukey's multiple comparisons test. H-K: MotiQ quantitative morphometry showing total area, spanned area, tree length, and ramification index. Data were measured by One-Way ANOVA followed by Tukey's multiple comparisons test. *** $p < 0.001$, **** $p < 0.0001$. N=11 per group for E-G. N=25-50 cells per group for H-K. ONH = optic nerve head.

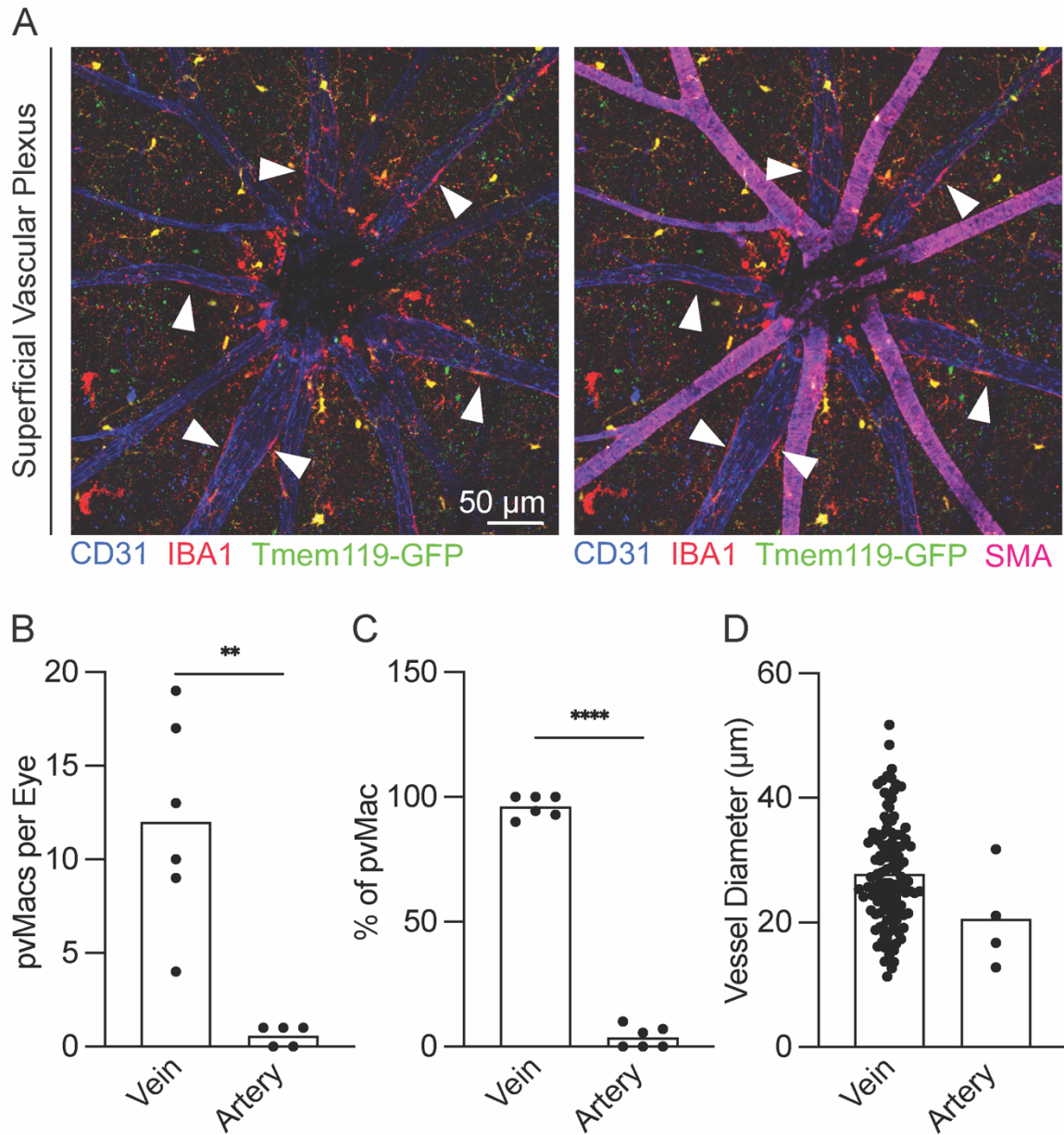


Figure 3. Perivascular macrophages reside on venules. A: Representative image of the superficial vascular plexus. White arrows identify perivascular macrophages (pvMac) on SMA^{neg} venules. B-C: Number and percent of pvMac on venules vs arterioles. D: Perivascular macrophages reside on vessels with an average diameter of 25-30 microns. Data were analyzed by paired two-tailed t-test: ** $p < 0.01$, **** $p < 0.0001$. N=5-6 mice per group (B-C). N=129 vein, 4 artery pvMacs (D).

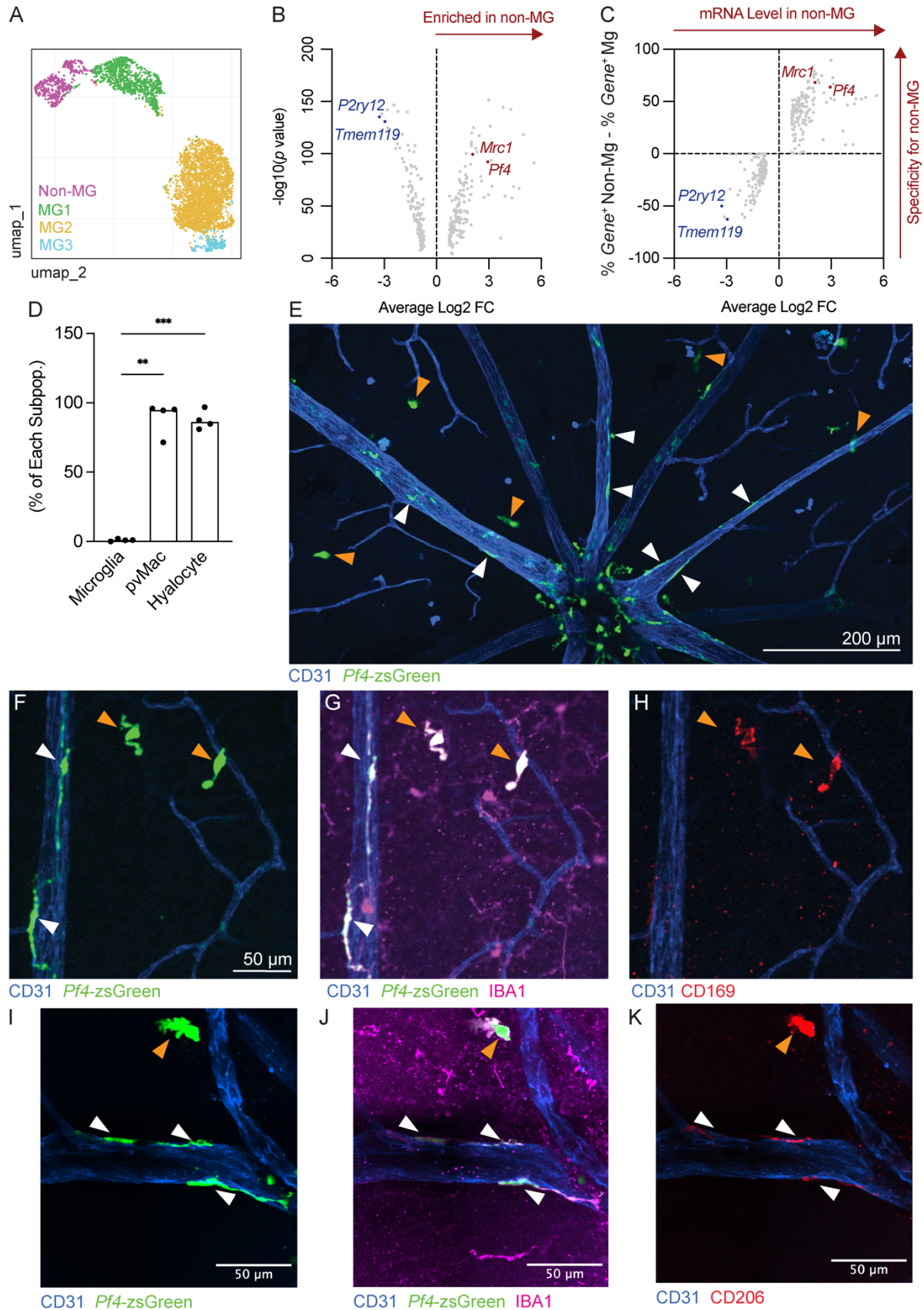
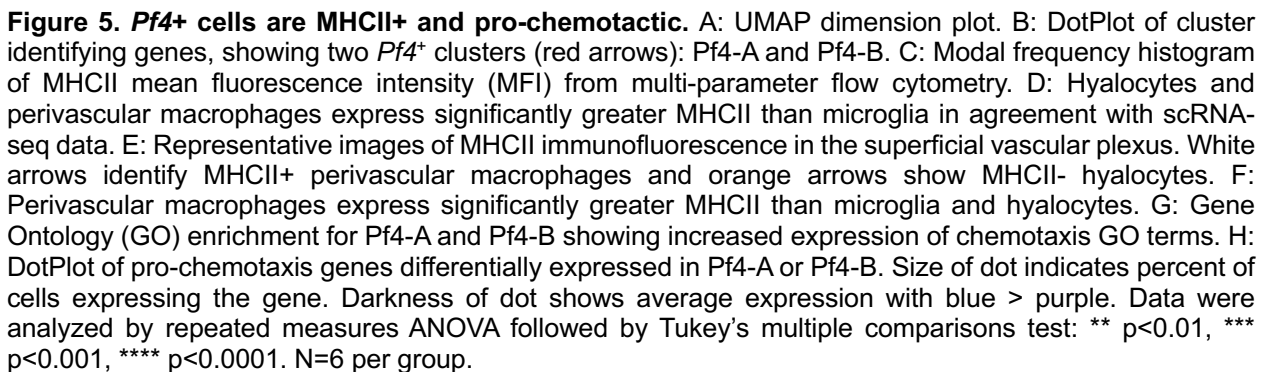


Figure 4. Perivascular macrophages express *Pf4*. A: UMAP dimension plot. B-C: Microglia (MG) express greater *P2ry12* and *Tmem119* than non-MG. *Mrc1* and *Pf4* are more highly expressed in non-MG retinal macrophages. D: Representative image of the superficial vascular plexus. Orange arrows delineate CD169⁺ hyalocytes. White arrows identify perivascular macrophages (pvMac). E: Perivascular macrophages and hyalocytes were targeted by *Pf4*^{Cre} significantly greater than microglia. Data were analyzed by repeated measures ANOVA followed by Tukey's multiple comparisons test: ** p<0.01, *** p<0.001. F-H: Representative zoomed in images of *Pf4*-zsGreen perivascular macrophages and hyalocytes stained with CD169 (F-H) or CD206 (I-K). N=4 per group for D. Images in F-K are representative from 3 mice.



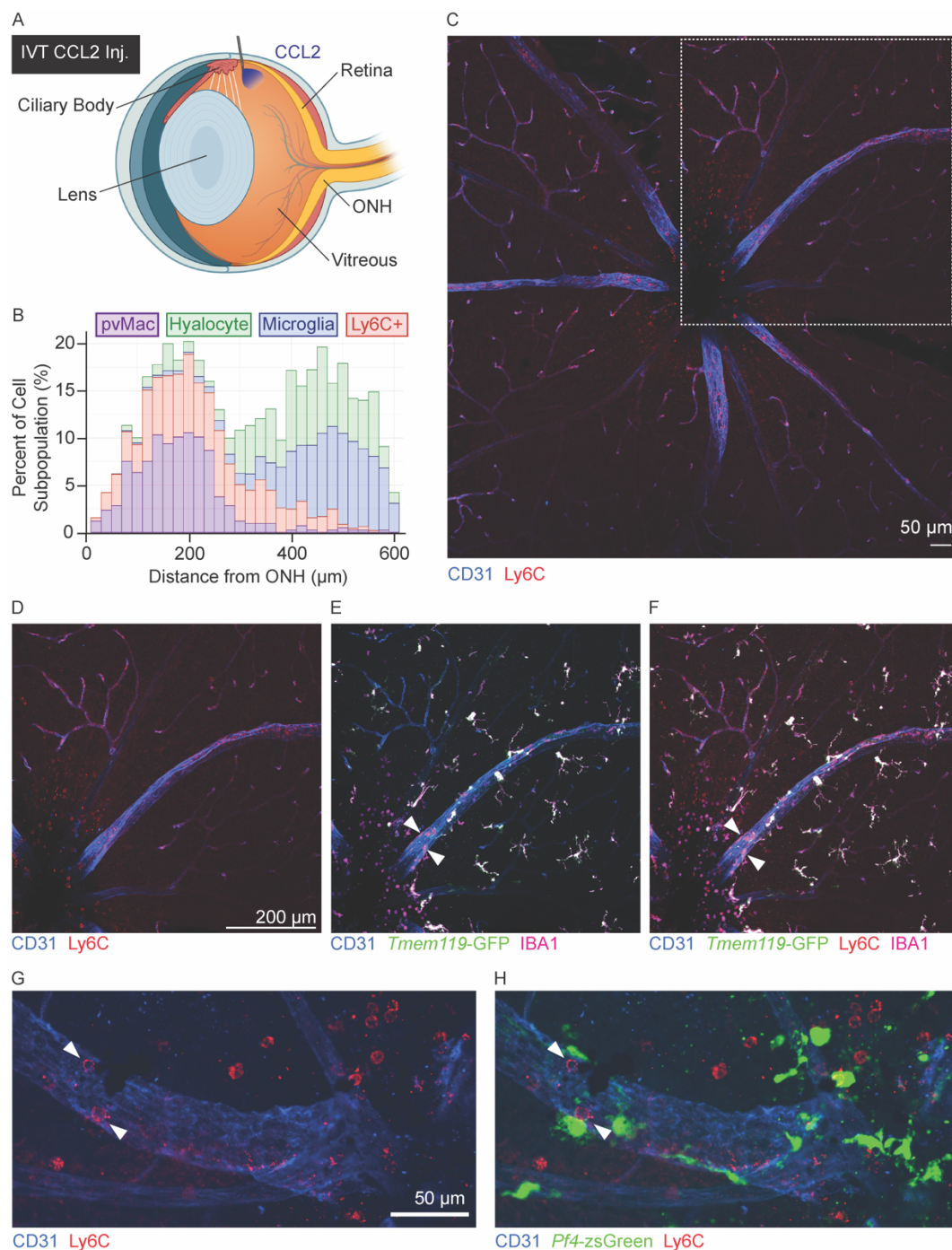


Figure 6. Perivascular macrophages correlate with Ly6C⁺ inflammatory cell infiltration. A: Schematic showing approximate location for intravitreal injections of CCL2. B: Frequency histogram of each cell type and their distance from the optic nerve. Significant overlap was found between the distribution of perivascular macrophages and Ly6C⁺ cells using a transformation of the Kolmogorov-Smirnov test. N=2,998 cells. C: Overview representative image of Ly6C⁺ cell infiltration at the superficial vascular plexus. D-F: Zoomed in representative image identifying Ly6C⁺ cells close to the optic nerve head where most perivascular macrophages (white arrowheads) reside in Tmem119^{GFP} mice. G-H: Zoomed in representative image of Pf4-zsGreen mice showing close association between Ly6C⁺ monocytes (red cell, white arrowhead) and Pf4⁺ perivascular macrophages.

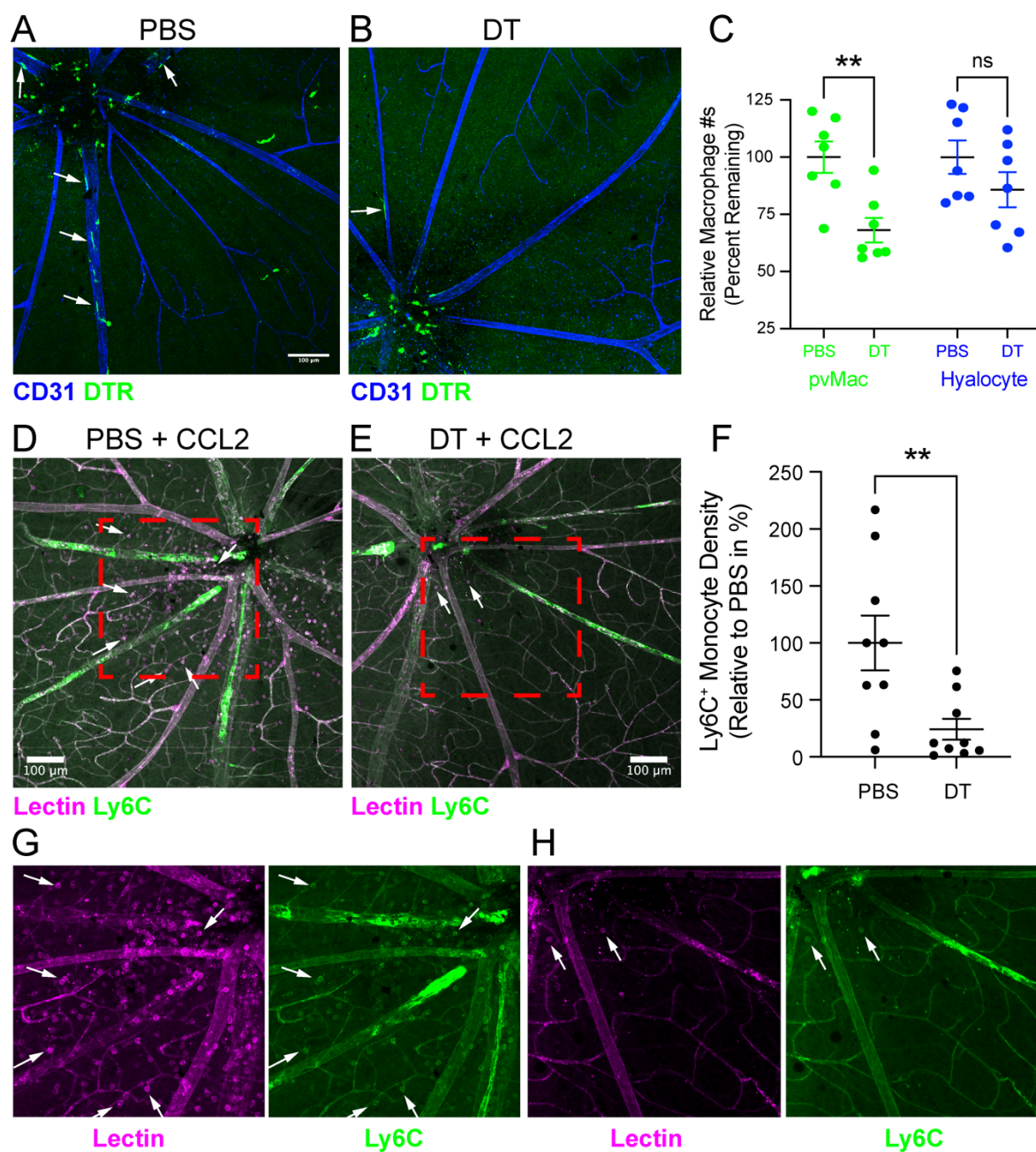


Figure 7. *Pf4-DTR* mice deplete perivascular macrophages and block immune cell infiltration. A-B: Representative immunofluorescence images of the superficial vascular plexus from PBS and DT (diphtheria toxin) treated *Pf4^{Cre} :: Rosa26^{CAG-LSL-DTR}* mice. White arrows identify DTR⁺ (diphtheria toxin receptor) perivascular macrophages. C: DT treatment reduces the number of perivascular macrophages without affecting hyalocytes. Data were analyzed by two-way ANOVA followed by Sidak's multiple comparisons test: ns = not significant, ** $p < 0.01$. N=7 per group. D-E: Representative immunofluorescence images of the superficial vascular plexus from PBS and DT treated *Pf4^{Cre} :: Rosa26^{CAG-LSL-DTR}* mice after intravitreal CCL2 injection. White arrows identify Ly6C⁺ infiltrating immune cells. Red hashed boxes indicate enlarged areas in G-H. F: DT treatment decreases the density of Ly6C⁺ monocytes after CCL2 injection. Data were analyzed by Mann-Whitney test because the distribution was non-parametric on the Shapiro-Wilk test: ** $p < 0.01$. N=9 per group. G-H: Enlarged images from D-E separated by Lectin and Ly6C channels for PBS (G) and DT (H) treatment.